J Neurosurg Spine 16:289–295, 2012

Three-dimensional measurement of growth of ossification of the posterior longitudinal ligament

Clinical article

Takahito Fujimori, M.D.,[1] Motoki Iwasaki, M.D., Ph.D.,[1] Yukitaka Nagamoto, M.D.,[1] Takahiro Ishii, M.D., Ph.D.,[2] Hironobu Sakaura, M.D., Ph.D.,[3] Masafumi Kashii, M.D., Ph.D.,[1] Hideki Yoshikawa, M.D., Ph.D.,[1] and Kazuomi Sugamoto, M.D., Ph.D.[4]

Departments of [1]Orthopedic Surgery and [4]Orthopedic Biomaterial Science, Osaka University Graduate School of Medicine; [2]Department of Orthopedic Surgery, Kaizuka City Hospital, Osaka; and [3]Department of Orthopedic Surgery, Kansai Rosai Hospital, Hyogo, Japan

Object. Ossification of the posterior longitudinal ligament (OPLL) is a progressive disease that causes cervical myelopathy. Because 2D evaluation of ossification growth with plain lateral radiographs has limitations, the authors developed a unique technique to measure ossification progression and volume increase by using multidetector CT scanning.

Methods. The authors used serial thin-slice volume data obtained by multidetector CT scanning in 5 patients. The mean patient age was 63 years, and the mean follow-up duration was 3.1 years. First, a 3D model of OPLL was semiautomatically segmented at a specific threshold. Then, a preoperative model of OPLL was superimposed on a postoperative model using voxel-based registration of the vertebral bodies. Progression and volume increase were measured using a digital viewer that was developed by the authors. Progression was visualized using a color-coded contour on the surface of the OPLL model.

Results. All patients had progression of 0.5 mm or greater. The mean values concerning OPLL growth were as follows: maximum progression length, 4.7 mm; progression rate, 1.5 mm/year; volume increase, 1622 mm^3; volume expansion rate, 37%; and volume increase rate, 484 mm^3/year. The accuracy of superimposition by voxel-based registration, defined as closeness to the true value, was less than 0.31 mm. For intraobserver reproducibility of the volume measurement, the mean intraclass correlation coefficient, root mean square error, and coefficient of variation were 0.987, 16.0 mm^3, and 1.7%, respectively.

Conclusions. Ossification of the posterior longitudinal ligament progresses even after surgery. Three-dimensional evaluation with the aid of CT scans is a useful and reliable method for assessing that growth.
(DOI: 10.3171/2011.11.SPINE11502)

Key Words • **ossification** • **posterior longitudinal ligament** • **three-dimensional** • **volume increase** • **progression** • **voxel-based registration** • **growth**

Ossification of the posterior longitudinal ligament is a progressive disease with ectopic bone formation in the spinal canal.[4,7,17] Surgical invasion, young age, and type of OPLL have been reported to be risk factors for progression.[2,10] However, the course of natural progression is still unclear, because OPLL grows slowly, by the millimeter. Previous studies have reported documentation of the progression of OPLL by plain radiography.[1,2,5,6] To the best of our knowledge, however, there have been no reports of 3D evaluation of OPLL growth. We developed a unique technique to evaluate growth three-dimensionally using multidetector CT scanning. We then conducted a study to determine the validity of our technique.

Abbreviations used in this paper: CV = coefficient of variation; ICC = intraclass correlation coefficient; OPLL = ossification of the posterior longitudinal ligament; RMSE = root mean square error.

Methods

Data Source

We evaluated thin-slice CT volume data, available at more than 2-year intervals, that had been obtained in 5 patients. All patients had a history of surgery for cervical OPLL; we had access to CT volume data for OPLL before

and after surgery for all of them. For all patients, an open-door laminoplasty was performed, using 2 graft bones as spacers. The CT scans were obtained using a commercial CT system (LightSpeed, General Electric) with a slice thickness of 0.625 mm and a pixel size of 0.352 × 0.352 mm. The data were transferred via a DICOM (digital imaging and communications in medicine) network into a computer workstation, where image processing was performed using Virtual Place software (M series, Medical Imaging Laboratory). All protocols for this retrospective study were approved by our institution's review board.

Measurement of Progression and Volume Increase

Measurement of progression and volume increase consisted of 3 stages. First, each vertebra with OPLL was semiautomatically extracted at a specific threshold, using a process known as segmentation. A window width of 2000 HU and window level of 150 HU were used for the threshold, as has been done in earlier studies.[8,12] Second, the preoperative model of the vertebral body was superimposed over the postoperative model of the same vertebral body to obtain a matrix that represents migration. This superimposition is possible because after removal of the OPLL and opening of the lamina, the vertebral body can be regarded as a rigid body that does not vary from before surgery to after surgery. By this matrix, the OPLL attached to the vertebra was accurately superimposed (Fig. 1). Third, the progression length and volume increase between preoperative OPLL and postoperative OPLL was assessed with the original digital viewer (Orthopedic Viewer, Osaka University). Progression was visualized in color-coded contour at 0.5- or 1-mm intervals on the bone surface for better understanding. In measuring OPLL volume, it was difficult to determine the boundary between the OPLL and the vertebral body. Therefore, preoperative and postoperative OPLL models were extracted from the superimposed vertebrae in the same margin bounded by the rectangle, with bilateral inflection points between the vertebral body and pedicle as vertices (Fig. 2). The expansion rate (volume increase divided by prevolume) was also assessed.

Accuracy of Voxel-Based Registration

Voxel-based registration is a method for determining the relative positions of 3D models at different coordinates, using a corresponding method that is based on the correlation between CT values of each voxel.[9] This calculation is performed using software, and the relative positions are represented as a matrix. This matrix is converted to 6 df by Euler angles, with the sequence of yaw (Y), pitch (X), roll (Z), and translations, using a previously defined coordinate system[9] (Fig. 1). We performed in vitro validation of the accuracy of our experimental CT method for the cervical spine using fresh-frozen vertebrae. More than 8 tantalum beads with a radius of 1.0 mm were implanted in the vertebrae. Subsequently, CT scans were obtained 8 times in different positions with the same imaging parameters. Each vertebra was then superimposed by voxel-based registration. The true value of the

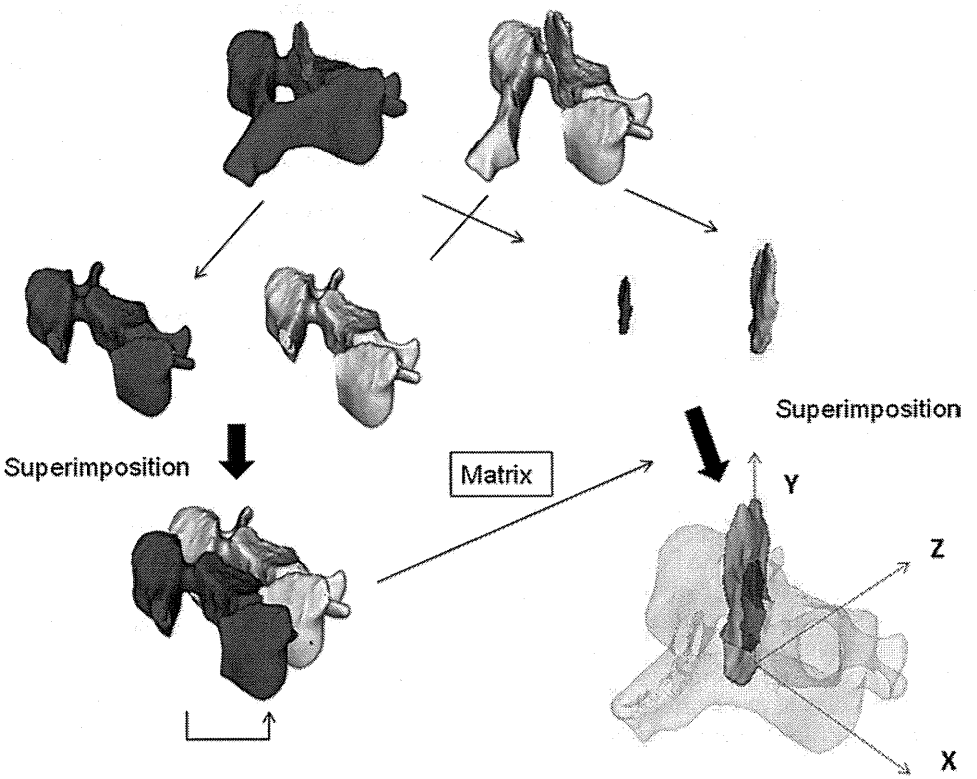

Fig. 1. Superimposition of OPLL by voxel-based registration. Three-dimensional models of OPLL before and after surgery were segmented together with the vertebral bodies. They were superimposed on the matrix derived from voxel-based registration of the vertebral bodies. This matrix is converted to 6 df by Euler angles, with the sequence of yaw (Y), pitch (X), roll (Z), and translations.

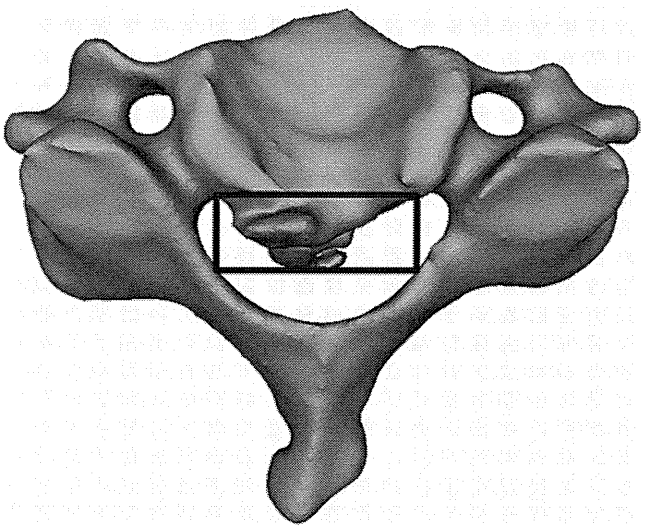

FIG. 2. The volume of OPLL was defined as the area bounded by the rectangle.

migration was measured by marker-based registration, providing gold-standard data. Accuracy was defined as the closeness to the true value; the RMSE was assessed.

Reproducibility of Volume Measurement

To assess reproducibility of measurement of OPLL volume, 3 observers measured the volume of 10 OPLL segments twice with 1 week elapsing between each measurement. Intraobserver and interobserver ICC, RMSE, and CV were assessed.

Results

Clinical Data

The mean patient age was 63 years (range 43–71 years), and the mean duration of follow-up monitoring was 3.1 years (range 2.1–3.8 years). The mean score on the Japanese Orthopaedic Association scale was 8.5 before surgery and 15.6 after surgery; the maximum possible score is 17. All patients experienced functional improvement after surgery. Four of the 5 patients had a mixed type of OPLL, and 1 had a localized type of OPLL (Table 1).

Progression of OPLL

Ossification of the posterior longitudinal ligament progressed 0.5 mm or greater in all patients. The average maximum progression length was 4.7 mm, and the progression rate was 1.5 mm/year (Table 1). The maximum progression occurred in the youngest patient (Case 1). Ossification of the posterior longitudinal ligament tends to grow actively around intervertebral areas and less in vertebral areas (Figs. 3 and 4).

Volume Increase of OPLL

The mean volume increase was 1622 mm^3 per patient, and the mean expansion rate was 37% during the follow-up period. The mean volume increase rate was 484 mm^3/year (Table 1).

Accuracy of Voxel-Based Registration and Reproducibility of Volume Measurement

The RMSE was 0.19° in flexion-extension, 0.13° in axial rotation, 0.21° in lateral bending, 0.13 mm in lateral translation, 0.15 mm in superoinferior translation, and 0.31 mm in anteroposterior translation (Table 2).

For intraobserver reproducibility of the volume measurement, the mean ICC, RMSE, and CV were 0.987, 16.0 mm^3, and 1.7%, respectively (Table 3). For interobserver reproducibility, the mean values were 0.968, 33.1 mm^3, and 3.4%, respectively (Table 4).

Illustrative Cases

Case 1

This 43-year-old man presented with a mixed type of OPLL. Before surgery, a plain lateral radiograph showed a continuous type of OPLL at the C2–3 level; however, the extent of OPLL at the C4–5 level was unclear (Fig. 3). Before surgery, the CT model clearly revealed a segmental type of OPLL at C-4, C-5, C-6, and C-7 (Fig. 4). Four years after laminoplasty, growth was apparent on radiographs; however, quantitative changes were unclear, especially at the levels of C-6 and C-7. The postoperative CT model revealed that the C3–4, C4–5, and C5–6 intervertebral spaces were bridged by growing OPLL. The ossified posterior longitudinal ligament behind the C-2

TABLE 1: Clinical data for 5 patients with OPLL*

Parameter	Case 1	Case 2	Case 3	Case 4	Case 5	Mean
age (yrs)	43	64	71	65	71	63
duration of follow-up monitoring (yrs)	3.6	2.6	3.5	2.1	3.8	3.1
JOA score (preop/postop)	7.5/15.5	9.5/17	8.5/15	6.5/14.5	10.5/16	8.5/15.6
OPLL type	mixed	localized	mixed	mixed	mixed	
progression length (mm)	8.9	6.4	3.6	2.5	2.1	4.7
progression rate (mm/yr)	2.4	2.5	1.0	1.2	0.6	1.5
vol increase (mm^3)	3851	369	2139	728	1022	1622
vol increase rate (mm^3/yr)	1056	143	608	346	268	484
expansion rate (%)	89	40	22	15	18	37

* JOA = Japanese Orthopaedic Association.

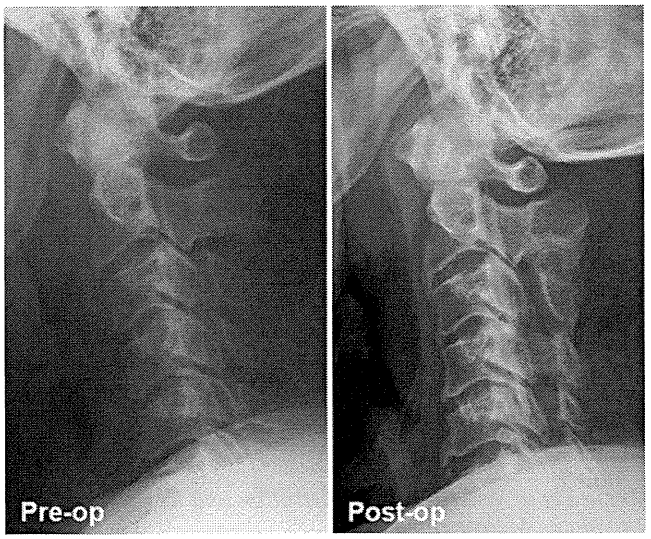

FIG. 3. Case 1. Plain lateral radiographs showing the mixed type of OPLL with the continuous type at C2–3 and the segmental type below C-2. However, it was difficult to recognize the segmental type of OPLL below the C-4 level on the preoperative radiograph.

vertebra had grown 8.9 mm cranially, and the volume increase was 769 mm^3. The ossified posterior longitudinal ligament of the C-4 vertebra had expanded; the volume increase was 977 mm^3. However, there was little progression in the C2–3 intervertebral space, which had already fused and had little mobility before surgery. The segmental type of OPLL at the C-6 level had grown only 1.2 mm, with a volume increase of 129 mm^3. Meanwhile, the segmental type of OPLL of the C-7 vertebra had grown 7.2 mm, with a volume increase of 708 mm^3. There was a big difference in growth between ossifications.

Case 2

This 64-year-old man with a localized type OPLL

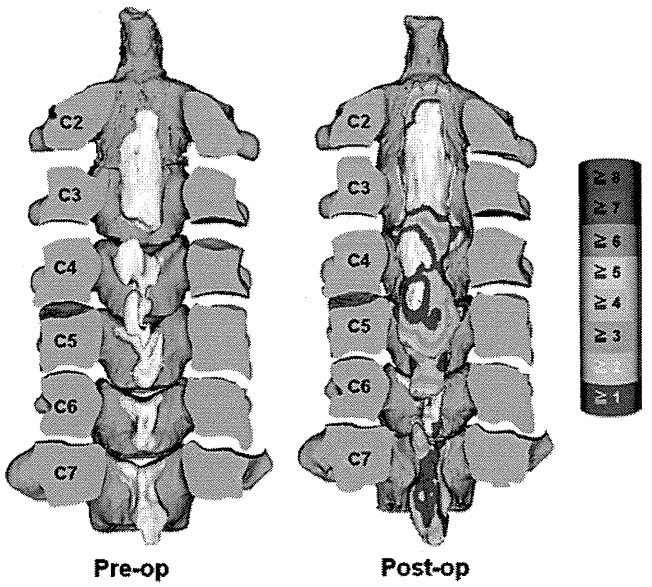

FIG. 4. Case 1. Three-dimensional models. The *bar* at the right shows the relationship between progression length and color.

TABLE 2: Accuracy of voxel-based registration of the cervical spine

Position	Rx (°)	Ry (°)	Rz (°)	Tx (mm)	Ty (mm)	Tz (mm)
1	0.26	0.08	−0.03	0.13	0.00	0.36
2	0.22	0.14	−0.11	−0.13	0.16	−0.30
3	0.06	0.08	0.29	0.10	0.03	0.41
4	−0.10	0.04	-0.28	0.02	0.07	−0.07
5	0.00	0.16	-0.09	0.13	−0.10	0.08
6	−0.21	−0.10	0.32	−0.17	0.34	0.14
7	−0.29	−0.25	−0.18	0.01	−0.05	0.58
8	0.17	0.08	−0.24	−0.19	0.12	−0.13
RMSE	0.19	0.13	0.21	0.13	0.15	0.31

* Rx = flexion-extension; Ry = axial rotation; Rz = lateral bending; Tx = lateral translation; Ty = superoinferior translation; Tz = anteroposterior translation.

underwent surgery. It was difficult to recognize OPLL on preoperative radiography (Fig. 5). However, CT scanning clearly revealed the OPLL attached to the C-4 vertebra (Fig. 6). Two years after laminoplasty, the OPLL had grown 6.4 mm in the cranial direction, with a volume increase of 369 mm^3.

Discussion

Advantages of CT Evaluation

Although several studies have reported on progression of OPLL, 2D evaluation with plain lateral radiographs has some limitations. Three-dimensional evaluation with CT scanning is better suited to measuring OPLL growth. For example, in the lower cervical spine, OPLL is likely to be masked by the shoulder girdle shadows. In young patients, OPLL may be less distinct because the ossification is less densely calcified. Although growth can occur in any direction, only craniocaudal and ventrodorsal progression are depicted on plain radiographs. Growth in the oblique direction is projected only orthographically onto a radiograph. Compared with radiography, CT scanning has several advantages. Computed tomography scanning is the most sensitive diagnostic method for detecting small ossifications or calcifications of the ligament, which are likely to be missed on radiographs.[15] However, conventional CT scanning also has the limitation of slice thickness. Measurement of OPLL on conventional radiographs is unreliable because the slice is likely to be thick, owing to the limited number of films used. It is also difficult to slice OPLL on the same level and angle to compare past and present

TABLE 3: Intraobserver reproducibility of volume measurement

Observer	ICC (95% CI)	RMSE (mm^3)	CV (%)
1	0.992 (0.970–0.998)	10.7	1.0
2	0.980 (0.928–0.995)	17.3	2.1
3	0.990 (0.962–0.998)	20.0	1.9
mean	0.987 (0.953–0.997)	16.0	1.7

TABLE 4: Interobserver reproducibility of volume measurement

Measurement	ICC (95% CI)	RMSE (mm^3)	CV (%)
1st	0.956 (0.842–0.989)	39.2	4.1
2nd	0.980 (0.919–0.995)	27.1	2.7
mean	0.968 (0.880–0.992)	33.1	3.4

ossification. However, these limitations can be overcome using helical scanning with multidetector CT and digital viewers. Additionally, accurate superimposition by voxel-based registration facilitates comparison of OPLL before and after surgery. The Orthopedic Viewer that we used was developed specifically for our study; however, the program was written using Visualization Toolkit (http://www.vtk.org/), an open-source free software system. Therefore, the measurement method that we used can be universally applied using similar viewers with equivalent function.

In our study, 3D evaluation, including volume increase, depicted minor changes in OPLL with high sensitivity. Hori et al.[5,6] reported that progression of greater than 2 mm on a plain radiograph occurred in 56.5%–75% of patients 2 years after laminoplasty. However, our method revealed that progression of greater than 0.5 mm occurred in all patients and that the mean rate of volume increase was 484 mm^3/year. Despite the growth of OPLL, myelopathy did not worsen in any patient in our study, partly because decompression was enough to forestall it. If enough space for the spinal cord can be obtained through laminoplasty, the growth of ossification could help decrease the dynamic factor and might not always be a clinical problem. However, the growth of OPLL after surgery could be a cause for revision surgery in some cases.[4,11,21] Fujiyoshi et al.[3] reported that additional fusion

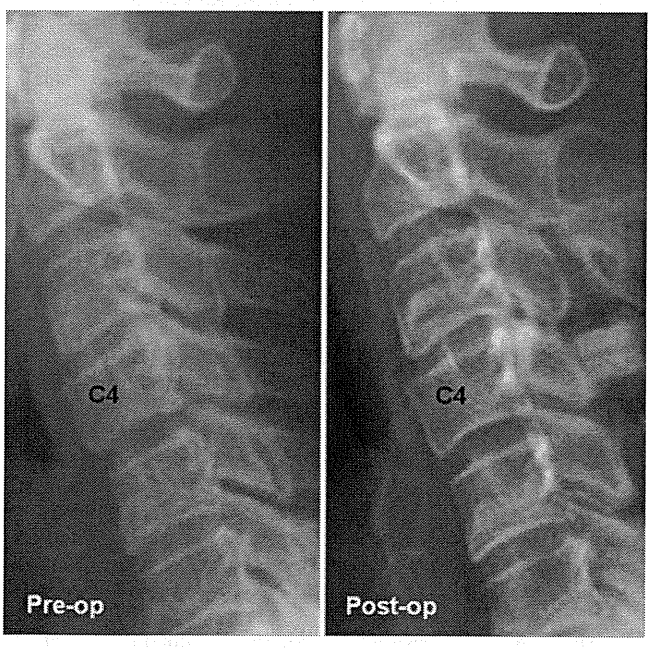

Fig. 5. Case 2. Plain lateral radiographs showing the localized type of OPLL at C-4. It was difficult to recognize ossification on the preoperative radiograph **(left)**. The postoperative radiograph **(right)** shows ossification; however, the length of progression was unclear.

for mobile segments in laminoplasty could slow the progression of OPLL. Ono et al.[16] reported that etidronate disodium had the potential to slow progression. Because OPLL is a kind of ectopic bone formation, some inhibitors of bone formation can prevent OPLL growth. It is essential to have an accurate and reliable measurement method to determine the efficacy of such drugs or of surgical procedures to decrease growth. The method that we used can be a useful tool for the future study of the natural progression process or the efficacy of drugs or surgery in treating OPLL.

Factors in Ossification Growth

Factors in ossification growth are roughly classified as either general or local. General factors include age, sex, and some hormonal factors, such as genetics, growth factors, and cytokines. It has been reported that collagen 11A2, collagen 6A1, bone morphogenetic protein–2, and transforming growth factor–β are related to progression of OPLL.[18,19] Local factors include mechanical stress, types of OPLL, and types of surgical procedures. Some researchers have reported that the segmental type of OPLL does not progress much in general.[2,5] Chiba et al.[2] reported that progression occurred in 53.3% of the continuous type of OPLL, 27.3% of the segmental type, 67.3% of the mixed type, and 40% of the localized type. They noted that the incidence of progression was significantly higher in patients younger than 59 years than in those older than 60 years. Hori et al.[5] reported that longitudinal progression occurred in 85% of the continuous type of OPLL, 29% of the segmental type, 100% of the mixed type, and 100% of the localized type. They also reported that thickening of ossifications occurred in 38% of the continuous type of OPLL, 0% of the segmental type, 41% of the mixed type, and 0% of the localized type.[6] They speculated that the pathological entity might be different for the continuous or mixed type of OPLL versus the segmental type. However, some reports of studies with longer follow-up periods noted that the segmental type of OPLL went on to become the continuous or mixed type of OPLL.[14,20] Murakami et al.[14] reported that the segmental type of OPLL had become the continuous type by 10 years of follow-up. They argued that the segmental type of OPLL was an initial stage of the continuous or the mixed type and that the entity was not different. Our findings correspond with those of Murakami et al.; however, we found that the extent of growth between OPLL types was considerably different even in the same patient (Case 1). It is not easy to explain these differences, because the growth process is not influenced by a single factor. However, one of the possible reasons for this is that the segmental type of OPLL located at the middle of a vertebral body grows slowly because it is not subjected to dynamic factors to the extent that OPLL in other locations is affected. Once the tip of an ossification reaches the intervertebral area, growth may be activated by increased dynamic factors. Hirabayashi et al.[4] reported that pseudarthrosis-like thickening occurred at mobile intervertebral spaces and that these changes stopped only after elimination of mobility. Our results correspond with theirs. In our study, ossifications grew actively in inter-

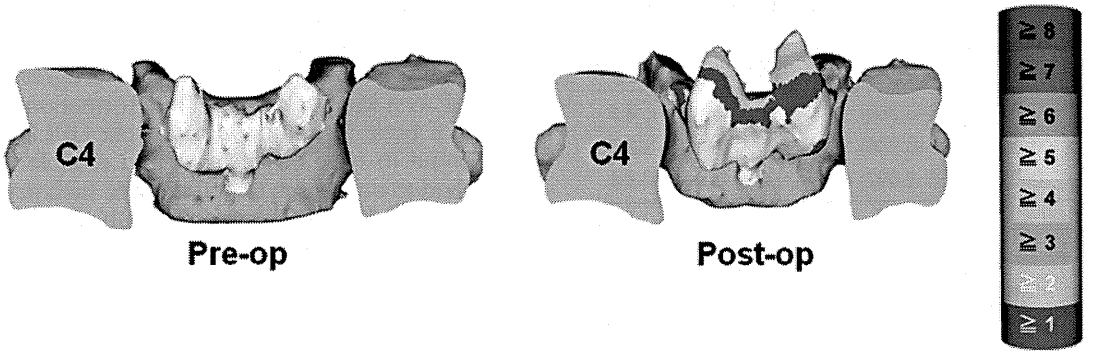

FIG. 6. Case 2. Three-dimensional models. The *bar* at the right shows the relationship between progression length and color.

vertebral areas as if they were bridging gaps to stabilize the mobile segments (Fig. 4). This finding suggests that dynamic factors are strongly involved in growth.[13] We speculate that the growth of OPLL decreases with the stabilizing effect of ossifications themselves and of laminoplasty.

In discussing the reasons for the different growth rates in different types of OPLL, the problem is the difficulty of detecting OPLL at its onset. A small ossification in the initial stage may sometimes be accidentally found, but most ossifications are found at a mature stage because a certain level of ossification must usually be attained before patients experience symptoms. Many studies have reported that ossifications do not grow at a constant speed but instead have growth spurts.[5,20] Therefore, it is theoretically possible that the mixed type of OPLL may be a form of the activated phase of the OPLL growth process. To answer these questions, long-term observation of OPLL starting from the initial stage is necessary. Our accurate 3D evaluation method can be an appropriate tool for further observation.

Conclusions

A novel 3D method for measuring OPLL growth, involving scanning by multidetector CT, showed that progression of greater than 0.5 mm occurred in all patients. After laminoplasty, the mean maximum progression rate was 1.5 mm/year, and the mean volume increase rate was 484 mm^3/year. This method can accurately detect changes in OPLL and thus can be a useful, reliable tool for examining OPLL growth.

Disclosure

This work was supported by a grant-in-aid from the Investigation Committee on Ossification of the Spinal Ligaments, Japanese Ministry of Public Health, Labor, and Welfare and a grant-in-aid for Scientific Research C (KAKENHI:22591632) from the Japan Society for the Promotion of Science. No benefits in any form have been or will be received from a commercial party related directly or indirectly to the subject of this manuscript.

Author contributions to the study and manuscript preparation include the following. Conception and design: Fujimori, Iwasaki, Ishii. Acquisition of data: Fujimori, Iwasaki. Analysis and interpretation of data: Fujimori, Nagamoto. Drafting the article: Fujimori. Critically revising the article: all authors. Reviewed submitted version of manuscript: all authors. Approved the final version of the manuscript on behalf of all authors: Fujimori. Statistical analysis: Fujimori. Administrative/technical/material support: Iwasaki, Yoshikawa, Sugamoto. Study supervision: Iwasaki, Yoshikawa, Sugamoto.

Acknowledgments

The authors thank Aya Sasaki. Katharine O'Moore-Klopf, E.L.S. (East Setauket, NY) provided professional English-language editing of this article.

References

1. Chiba K, Kato Y, Tsuzuki N, Nagata K, Toyama Y, Iwasaki M, et al: Computer-assisted measurement of the size of ossification in patients with ossification of the posterior longitudinal ligament in the cervical spine. **J Orthop Sci 10:**451–456, 2005
2. Chiba K, Yamamoto I, Hirabayashi H, Iwasaki M, Goto H, Yonenobu K, et al: Multicenter study investigating the postoperative progression of ossification of the posterior longitudinal ligament in the cervical spine: a new computer-assisted measurement. **J Neurosurg Spine 3:**17–23, 2005
3. Fujiyoshi T, Yamazaki M, Okawa A, Kawabe J, Hayashi K, Endo T, et al: Static versus dynamic factors for the development of myelopathy in patients with cervical ossification of the posterior longitudinal ligament. **J Clin Neurosci 17:**320–324, 2010
4. Hirabayashi K, Miyakawa J, Satomi K, Maruyama T, Wakano K: Operative results and postoperative progression of ossification among patients with ossification of cervical posterior longitudinal ligament. **Spine (Phila Pa 1976) 6:**354–364, 1981
5. Hori T, Kawaguchi Y, Kimura T: How does the ossification area of the posterior longitudinal ligament progress after cervical laminoplasty? **Spine (Phila Pa 1976) 31:**2807–2812, 2006
6. Hori T, Kawaguchi Y, Kimura T: How does the ossification area of the posterior longitudinal ligament thicken following cervical laminoplasty? **Spine (Phila Pa 1976) 32:**E551–E556, 2007
7. Hsieh PC, Wang MY: Introduction. Ossification of the posterior longitudinal ligament. **Neurosurg Focus 30(3):**Introduction, 2011
8. Inoue S, Goto S, Nagase J, Tanaka Y: Investigation of window width and window level of computed tomography for OPLL, in: **Annual Report of Taskforce of Research for Ossification of the Spinal Ligaments.** Tokyo: Japanese Ministry Of Public Health and Welfare, Vol 58, 1984, pp 237–239
9. Ishii T, Mukai Y, Hosono N, Sakaura H, Nakajima Y, Sato Y, et al: Kinematics of the upper cervical spine in rotation: in vivo three-dimensional analysis. **Spine (Phila Pa 1976) 29:** E139–E144, 2004
10. Iwasaki M, Kawaguchi Y, Kimura T, Yonenobu K: Long-term

results of expansive laminoplasty for ossification of the posterior longitudinal ligament of the cervical spine: more than 10 years follow up. **J Neurosurg 96 (2 Suppl):**180–189, 2002
11. Kawaguchi Y, Kanamori M, Ishihara H, Nakamura H, Sugimori K, Tsuji H, et al: Progression of ossification of the posterior longitudinal ligament following en bloc cervical laminoplasty. **J Bone Joint Surg Am 83-A:**1798–1802, 2001
12. Kokubun S, Sato T, Nishihira T: Computed tomography of the ossification of the spinal ligaments, in: **Seikeigeka Mook.** Tokyo: Kanehara Shuppan, Vol 50, pp 59–71, 1987
13. Matsunaga S, Sakou T, Taketomi E, Nakanisi K: Effects of strain distribution in the intervertebral discs on the progression of ossification of the posterior longitudinal ligaments. **Spine (Phila Pa 1976) 21:**184–189, 1996
14. Murakami M, Seichi A, Chikuda H, Takeshita K, Nakamura K, Kimura A: Long-term follow-up of the progression of ossification of the posterior longitudinal ligament. Case report. **J Neurosurg Spine 12:**577–579, 2010
15. Nagata K, Sato K: Diagnostic imaging of cervical ossification of the posterior longitudinal ligament, in Yonenobu K, Nakamura K, Toyama Y (eds): **OPLL: Ossification of the Posterior Longitudinal Ligament, ed 2.** Tokyo: Springer, 2006, pp 127–143
16. Ono K, Yonenobu K, Sako T, Kawai S, Nagata K: [Prevention of progression of ossification of the posterior longitudinal ligament (OPLL) by the administration of etidronate disodium (EHDP) after posterior decompression.] **Nippon Sekitsui Geka Gakkai Zasshi 9:**432–442, 1998 (Jpn)
17. Saetia K, Cho D, Lee S, Kim DH, Kim SD: Ossification of the posterior longitudinal ligament: a review. **Neurosurg Focus 30(3):**E1, 2011
18. Stapleton CJ, Pham MH, Attenello FJ, Hsieh PC: Ossification of the posterior longitudinal ligament: genetics and pathophysiology. **Neurosurg Focus 30(3):**E6, 2011
19. Stetler WR, La Marca F, Park P: The genetics of ossification of the posterior longitudinal ligament. **Neurosurg Focus 30(3):** E7, 2011
20. Terayama K, Ohtsuka K, Tsuama N, Ohtani K, Yamauchi Y, Yamaura I, et al: Investigation of ossification of the spinal ligaments with more than 5 years follow-up, in: **Annual Report of Taskforce of Research for Ossification of the Spinal Ligaments.** Tokyo: Japanese Ministry Of Public Health and Welfare, Vol 58, 1984, pp 85–96
21. Tokuhashi Y, Ajiro Y, Umezawa N: A patient with two resurgeries for delayed myelopathy due to progression of ossification of the posterior longitudinal ligaments after cervical laminoplasty. **Spine (Phila Pa 1976) 34:**E101–E105, 2009

Manuscript submitted June 2, 2011.
Accepted November 7, 2011.
Please include this information when citing this paper: published online December 16, 2011; DOI: 10.3171/2011.11.SPINE11502.
Address correspondence to: Takahito Fujimori, M.D., Department of Orthopedic Surgery, Osaka University Graduate School of Medicine, 2-2 Yamadaoka, Suita, Osaka 565-0871, Japan. email: takahito-f@hotmail.co.jp.

Infection and Immunity

Establishment of a Real-Time, Quantitative, and Reproducible Mouse Model of Staphylococcus Osteomyelitis Using Bioluminescence Imaging

Haruki Funao, Ken Ishii, Shigenori Nagai, Aya Sasaki, Tomoyuki Hoshikawa, Mamoru Aizawa, Yasunori Okada, Kazuhiro Chiba, Shigeo Koyasu, Yoshiaki Toyama and Morio Matsumoto

Infect. Immun. **2012, 80(2):733. DOI: 10.1128/IAI.06166-11. Published Ahead of Print 21 November 2011.**

IAI
Journals.ASM.org

Establishment of a Real-Time, Quantitative, and Reproducible Mouse Model of Staphylococcus Osteomyelitis Using Bioluminescence Imaging

Haruki Funao,[a] Ken Ishii,[a,f] Shigenori Nagai,[b,c] Aya Sasaki,[d] Tomoyuki Hoshikawa,[e] Mamoru Aizawa,[e,f] Yasunori Okada,[d] Kazuhiro Chiba,[a] Shigeo Koyasu,[b] Yoshiaki Toyama,[a] and Morio Matsumoto[a,f]

Department of Orthopaedic Surgery, School of Medicine, Keio University, Shinjuku, Tokyo, Japan[a]; Department of Microbiology and Immunology, School of Medicine, Keio University, Shinjuku, Tokyo, Japan[b]; Core Research for Evolutional Science and Technology (CREST), Japan Science and Technology Agency (JST), Tokyo, Japan[c]; Department of Pathology, School of Medicine, Keio University, Shinjuku, Tokyo, Japan[d]; Department of Applied Chemistry, School of Science and Technology, Meiji University, Ikuta, Kanagawa, Japan[e]; and Kanagawa Academy of Science and Technology (KAST), Kawasaki, Kanagawa, Japan[f]

Osteomyelitis remains a serious problem in the orthopedic field. There are only a few animal models in which the quantity and distribution of bacteria can be reproducibly traced. Here, we established a real-time quantitative mouse model of osteomyelitis using bioluminescence imaging (BLI) without sacrificing the animals. A bioluminescent strain of *Staphylococcus aureus* was inoculated into the femurs of mice. The bacterial photon intensity (PI) was then sequentially measured by BLI. Serological and histological analyses of the mice were performed. The mean PI peaked at 3 days, and stable signals were maintained for over 3 months after inoculation. The serum levels of interleukin-6, interleukin-1β, and C-reactive protein were significantly higher in the infected mice than in the control mice on day 7. The serum monocyte chemotactic protein 1 level was also significantly higher in the infected group at 12 h than in the control group. A significantly higher proportion of granulocytes was detected in the peripheral blood of the infected group after day 7. Additionally, both acute and chronic histological manifestations were observed in the infected group. This model is useful for elucidating the pathophysiology of both acute and chronic osteomyelitis and to assess the effects of novel antibiotics or antibacterial implants.

One of the most serious problems in the orthopedic field is infectious osteomyelitis, which causes progressive inflammation and destruction of bone tissue (19). Treatment of infectious osteomyelitis is challenging, because the pathogenic organisms and their drug sensitivities are variable. This problem is compounded by increasing numbers of drug-resistant bacterial strains, implant-associated infections, and elderly patients with compromised immune systems (18). Although progress has been made, controlling infectious osteomyelitis is still difficult. Therefore, experimental studies are warranted to develop more effective treatment options. A number of animal models of osteomyelitis have been reported (13, 26, 33, 35). However, many of them require sacrifice of the animals, and thus, they are limited in their availability for real-time assessments of the severity of infection and the efficacy of treatments. As a result, the pathophysiology of osteomyelitis remains poorly understood.

A recent development in optical imaging, bioluminescence imaging (BLI), permits the noninvasive sequential monitoring of cell growth and gene expression *in vivo*. This method allows real-time monitoring of implanted cells in live animals (16, 27). Inoculated bacteria that emit a constant bioluminescent signal can be detected through the tissues of a live animal using an ultrasensitive, cooled, charge-coupled device (CCD) camera. This approach has proven useful in studies in the fields of oncology (38), endocrine disruptors (28), metabolism (37), hematopoietic cells (41), regenerative medicine (16, 27), immunology (6, 21), and infections (2, 5, 11, 14, 20, 24, 34, 42).

Previous models of infectious diseases required sacrifice of animals to quantify the bacteria by culturing tissue specimens. In contrast, the BLI technique monitors bacterial growth throughout the course of infection in real time without sacrificing animals. To our knowledge, there is no previous model in which infectious processes in bone from the acute to the chronic phases were evaluated using BLI, as well as the kinetics of immune cells and the levels of cytokines/chemokines in serum. The purpose of the present study was to establish a real-time, quantitative, and reproducible mouse model of osteomyelitis using the BLI technique.

MATERIALS AND METHODS

Bioluminescent bacteria. A bioluminescent strain of *Staphylococcus aureus*, Xen-29, was obtained from Caliper LS Co. (Hopkinton, MA) and cultured in Luria Bertani medium (Sigma-Aldrich Co., St. Louis, MO) at 37°C under ambient aeration with gentle agitation. The bacteria were selectively grown in medium containing 200 μg/ml kanamycin. *S. aureus* Xen-29, derived from the parental strain ATCC 12600, has a stable copy of a modified *Photorhabdus luminescens luxABCDE* operon, encoding enzymes responsible for the luminescent reaction. Bacterial bioluminescence requires no substrate to be added to generate the light and will constitutively emit a bioluminescent signal as long as the organism is viable. The bacterial samples were frozen and stored at −80°C. The samples were thawed at 4°C for 1 h prior to each experiment. Typically, bacterial viability was maintained at 4°C for approximately 5 h after thawing.

Mouse osteomyelitis model. Eighteen BALB/c adult male mice (12 weeks old; 20 to 25 g) purchased from Sankyo Labo Service (Shizuoka,

Received 10 November 2011 Accepted 10 November 2011
Published ahead of print 21 November 2011
Editor: A. J. Bäumler
Address correspondence to Ken Ishii, ishii-km@sc.itc.keio.ac.jp.

doi:10.1128/IAI.06166-11

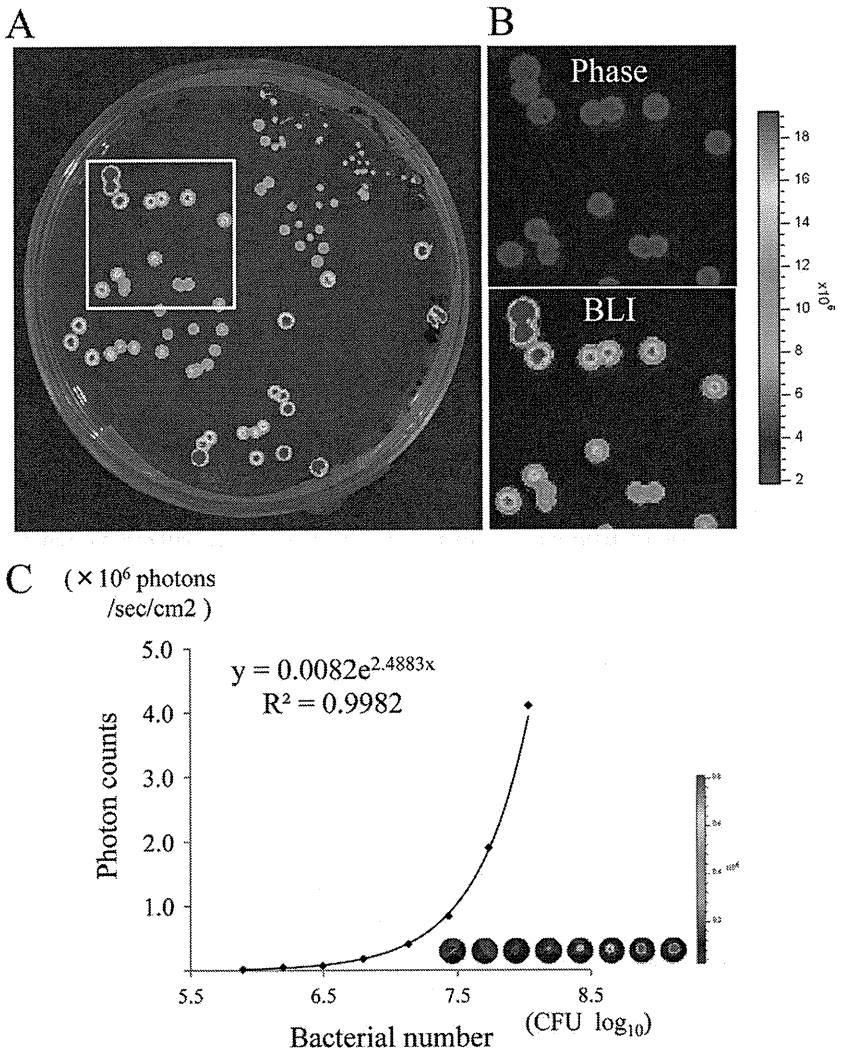

FIG 1 Correlation between bacterial number and bacterial photon intensity *in vitro*. Photon emission of the bacterial bioluminescent signals of *S. aureus* strain Xen-29 was captured as false-color photon count images and quantified by a BLI system. To examine the sensitivity of the BLI, a CCD-based macroscopic detector was used to quantify the bacterial PI (photons/s/cm^2/sr) at various bacterial numbers (7.8×10^5 to 1.0×10^8 CFU per well). Bioluminescent signals were detected from colonies of bioluminescent *S. aureus in vitro* (A and B), and there was a significant correlation between the number of bacterial CFU and the bacterial PI *in vitro* ($R^2 = 0.998$) (C).

Japan) were used in this study. The mice were maintained in our animal facility under specific-pathogen-free conditions. The mice were anesthetized with an intraperitoneal injection of 50 mg of pentobarbital/kg of body weight, and the skin on the left knee was shaved and sterilized with povidone iodine. A skin incision was made over the left knee, and the distal femur was exposed through a lateral parapatellar arthrotomy with medial displacement of the quadriceps-patellar complex. The distal end of the femur was perforated using a high-speed drill with a 0.5-mm sharp steel burr (Fine Science Tools Inc., Foster city, CA). Then, a channel was created using a 23-gauge (external diameter, 0.6 mm) needle, through which the bioluminescent strain of *S. aureus* (1.0×10^8 CFU) in 1 μl of medium was inoculated into the medullary cavity of the femur using a Hamilton syringe. Phosphate-buffered saline (PBS) was administered to the control group using the same technique. The burr hole was closed with bone wax, the dislocated patella was reduced, and the muscle and skin openings were closed by sutures. The animals were placed on a heating pad and carefully monitored until recovery. The observation of spontaneous forelimb movement and the drinking of water were the criteria used to determine that the animals had recovered from the anesthesia.

To measure and analyze the bacterial bioluminescent signal by BLI, the mice were anesthetized via inhalation of aerosolized isoflurane mixed with oxygen. The animals were laid on their backs and imaged for 5 min. All experiments were approved by the Animal Care and Use Committee of Keio University.

BLI. A Caliper LS-Ivis Lumina cooled CCD optical macroscopic imaging system (Summit Pharmaceuticals International Co., Tokyo, Japan) (30) was used for the BLI. Photon emissions of the bacterial bioluminescent signal were captured, converted to false-color photon count images, and quantified with Living Image version 3.0 software (Caliper LS Co., Hopkinton, MA). The bacterial photon intensity (PI) was expressed as photon flux in units of photons/s/cm^2/sr. To quantify the bacterial luminescence, regions of interest (ROIs) were defined in the bacterial plates or inoculated areas and examined. To evaluate the luminescence expression of the bacteria, we first examined whether various numbers of bacteria correlated with the bacterial PI *in vitro* and *in vivo*. To analyze the time course of the infection *in vivo*, the bacterial PI in an ROI was sequentially measured on days 1, 3, 7, 14, and 21 after the operation.

Serological evaluation. Blood samples were collected from the infected and the control mouse groups by retro-orbital bleeding before surgery (day 0) and on days 0.5 (12 h), 1, 3, 7, 14, and 21 after the operation.

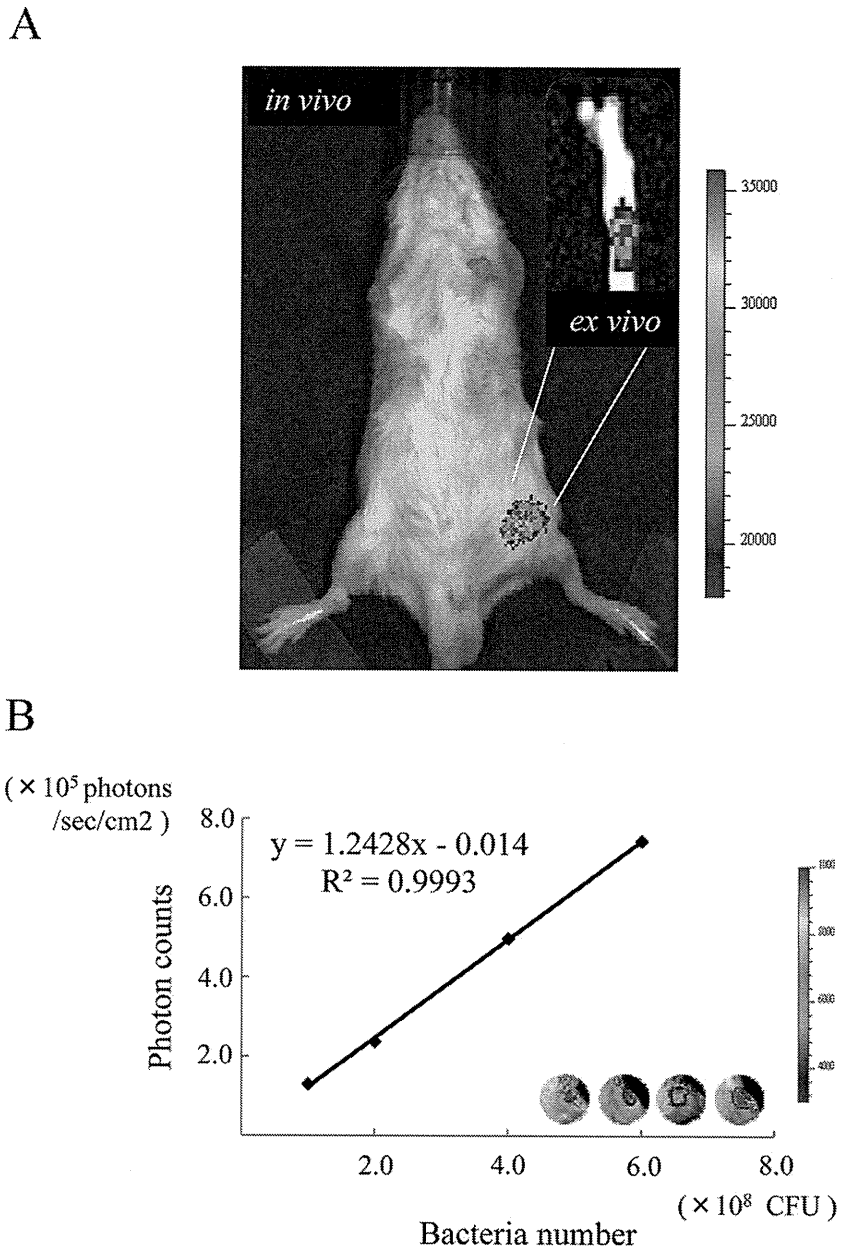

FIG 2 Correlation of bacterial number and bacterial photon intensity *in vivo*. (A) During *ex vivo* imaging, the bacterial bioluminescent signal was detected only in the medullary cavity of the femur and not in the surrounding tissue. (B) Different amounts of bacteria (1.0×10^8 to 6.0×10^8 CFU per inoculation) were inoculated into the femurs, and the bioluminescence in the ROIs was monitored by the BLI system. Significant correlation was observed between the inoculated bacterial number and the bacterial PI *in vivo* ($R^2 = 0.999$).

To measure inflammatory cytokines and chemokines, the sera of both groups were serially diluted, and interleukin-6 (IL-6), IL-1β, C-reactive protein (CRP), and monocyte chemotactic protein 1 (MCP-1) were measured by using enzyme-linked immunosorbent assay (ELISA) kits (R&D Systems, Minneapolis, MN; Kamiya Biomedical Co., Seattle, WA). Detection was carried out according to the manufacturers' instructions.

Flow cytometry. Peripheral blood samples from the infected and the control mice were subjected to double immunofluorescence staining and analyzed by flow cytometry on days 1, 3, 7, 14, and 21 after the operation. Fluorescein isothiocyanate (FITC)–anti-CD11b (clone M1/70) and phycoerythrin (PE)–anti-Ly-6C (Gr-1) (clone RB6-8C5) antibodies (Abs) were purchased from BD Biosciences (San Diego, CA). To block the nonspecific binding of Abs to Fc receptors, the isolated cells were incubated with an anti-CD16/32 monoclonal Ab (MAb) (clone 2.4G2; 1:250) at 4°C for 20 min. The cells were then stained with a mixture of fluorochrome-labeled MAbs at 4°C for 20 min, washed, and incubated with 7-aminoactinomycin D (1:500; BD Biosciences, San Diego, CA) at 4°C for 5 min. Flow cytometry was performed on a FACSCalibur (BD Biosciences, San Diego, CA), and the data were analyzed with FlowJo software (Tree Star, Ashland, OR). Murine granulocytes were defined as SSC^{high} (1× side scatter is 0.15 M NaCl plus 0.015 M sodium citrate) $CD11b^+$ cells (29). These cells also expressed Gr-1 (not shown).

Histological analysis. Femur specimens were collected and analyzed histologically on days 3, 7, 21, and 28 after the operation in both groups. The mice were sacrificed, and the femurs were removed and separated from the soft tissues. The samples were fixed in 4% paraformaldehyde and

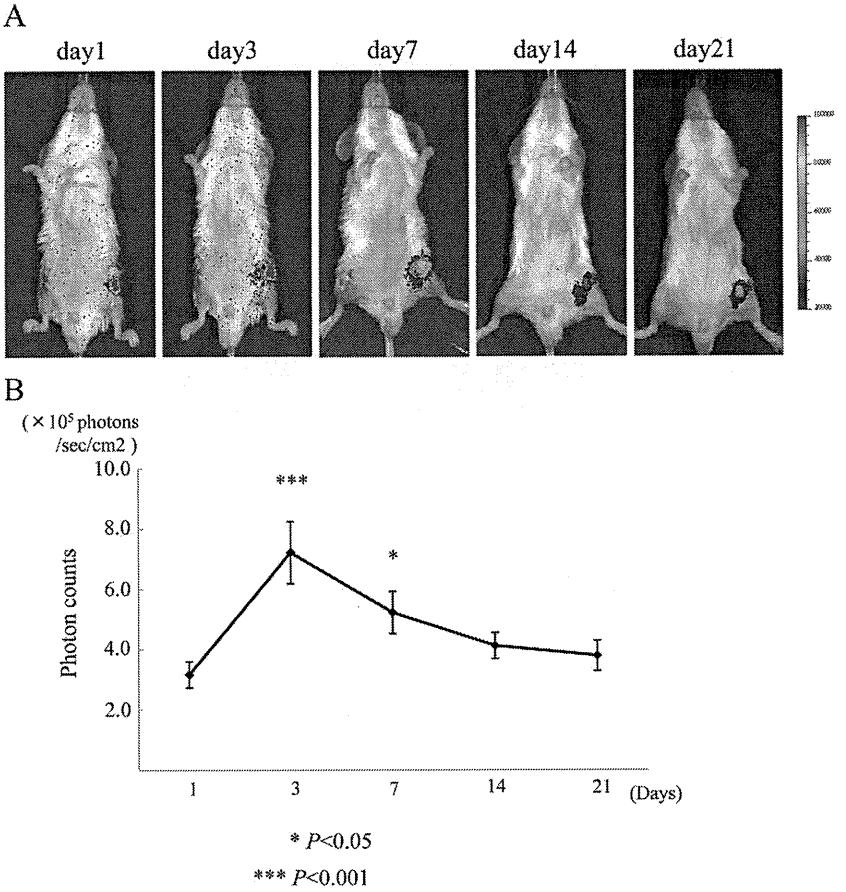

FIG 3 Time course changes of bacterial photon intensity in the mouse osteomyelitis model. *S. aureus* strain Xen29 (1.0×10^8 CFU) in 1 μl of medium was inoculated into the medullary cavity of the femur. The bacterial PI from an ROI was then sequentially measured on days 1, 3, 7, 14, and 21 after surgery ($n = 6$ for each time point). The mean bacterial PI in the infected group peaked on day 3 ($7.2 \times 10^5 \pm 1.0 \times 10^5$ PI) and remained at a high level until approximately day 7 ($5.2 \times 10^5 \pm 0.7 \times 10^5$ PI). Shown are means ± standard errors of the mean (SEM).

demineralized with EDTA. The samples were then embedded in paraffin, cut into 5-μm-thick sections, and stained with hematoxylin and eosin or Gram stain.

Statistical analysis. Correlations between the bacterial CFU and the bacterial PI *in vitro* and *in vivo* were analyzed by linear regression. Changes in the bacterial PI in the infected group were analyzed with Student's *t* test. One-way analysis of variance (ANOVA) and the Fisher *post hoc* test were used to compare the levels of IL-6, IL-1β, CRP, and MCP-1 in serum and the proportion of granulocytes in the peripheral blood between the two groups. Correlation between the bacterial PI and the serum CRP levels was determined using Pearson's correlation coefficient. SPSS II software (IBM-SPSS, Tokyo, Japan) was used, and a *P* value of less than 0.05 was considered significant in all the statistical analyses.

RESULTS

Correlation between bacterial number and bacterial photon intensity *in vitro*. A bioluminescent signal that was sufficient to yield a significant value over background was detected by the BLI system from a single colony of the bioluminescent strain *S. aureus* Xen-29 cultured in Luria Bertani medium (Fig. 1A and B). To examine the sensitivity of the BLI, we used a CCD-based macroscopic detector to measure the PI of bacterial samples with 7.8×10^5 to 1.0×10^8 CFU/well. A minimum of 7.8×10^5 CFU of bacteria was sufficient to produce a detectable signal above the background noise. This quantitative bioluminescence analysis revealed that there was a significant correlation between the number of bacterial CFU and the bacterial PI *in vitro* ($R^2 = 0.998$) (Fig. 1C). To confirm that only live *S. aureus* naturally emitted the luminescent signals, colonies of *S. aureus* bacteria fixed with 4% paraformaldehyde were visualized with the BLI system. No signal was detected from the fixed bacteria (data not shown).

Correlation between bacterial number and bacterial photon intensity *in vivo*. To visualize the infected site *ex vivo*, immediately after the intrafemural inoculation of *S. aureus*, the infected femur was removed and separated from the soft tissues, and the exposed femur was monitored by the BLI system. The bacterial bioluminescent signals were detected only in the medullary cavity of the femur and not in the surrounding tissue (Fig. 2A). To examine whether the number of inoculated bacteria correlated with the bacterial PI *in vivo*, we performed inoculations with different numbers of bacteria (1.0×10^8 to 6.0×10^8 CFU per inoculation) and measured the bacterial PI. As shown in Fig. 2B, there was a significant correlation between the number of inoculated bacteria and the bacterial PI ($R^2 = 0.999$).

Time course of bacterial photon intensity in the mouse OM model. Immediately after the inoculation of *S. aureus* (1.0×10^8 CFU) in 1 μl of medium into the femur, stable luminescent signals were observed in all the animals. Sequential analyses of the bacte-

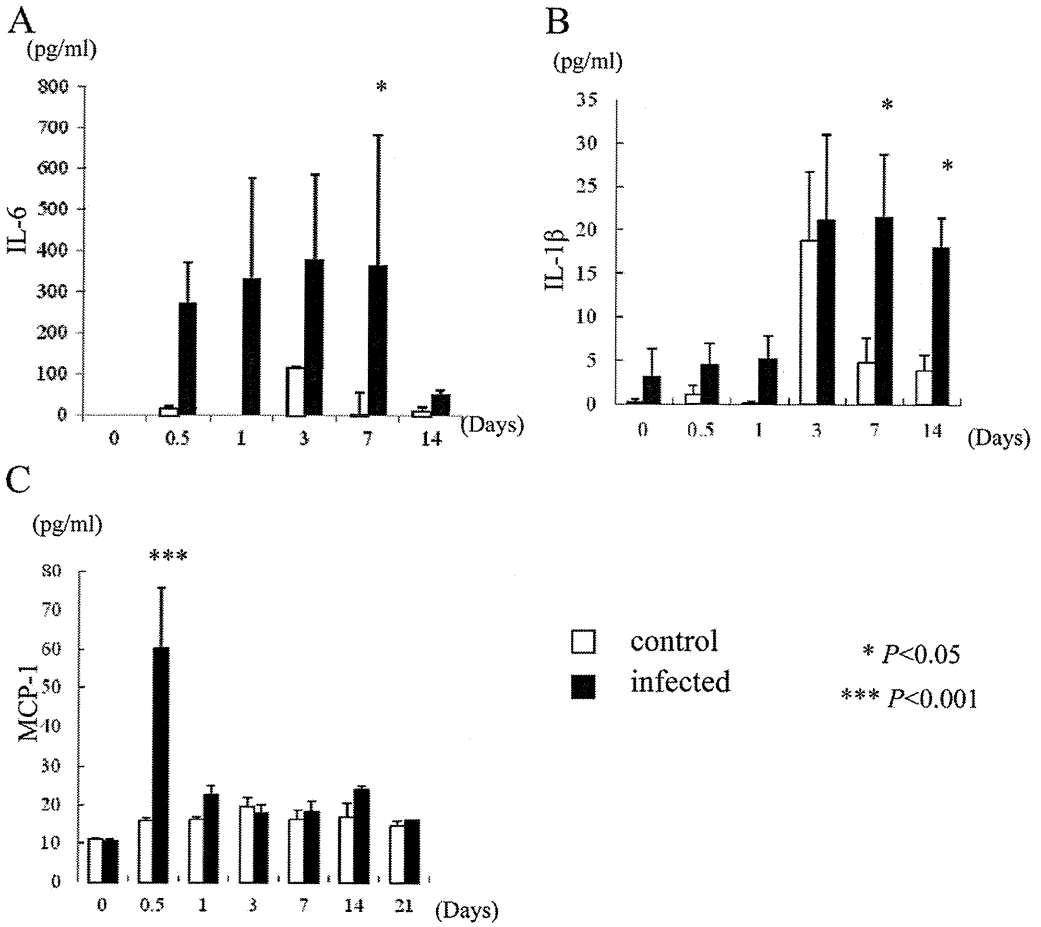

FIG 4 Serological evaluation of control and infected groups. Blood samples from the site of retro-orbital bleeding were collected from the mice before surgery (day 0) and on days 0.5 (12 h), 1, 3, 7, 14, and 21 after the operation in the infected and the control groups ($n = 3$ each). The serum IL-6 (A), IL-1β (B), and MCP-1 (C) levels were measured with ELISA kits. Shown are means ± SEM.

rial luminescence revealed that the mean bacterial PI in the infected group peaked on day 3 ($7.2 \times 10^5 \pm 1.0 \times 10^5$ PI) and remained at a high level until approximately day 7 ($5.2 \times 10^5 \pm 0.7 \times 10^5$ PI) (Fig. 3). Notably, the strong bacterial bioluminescent signal was detected only at the injection site of the femur, and the surrounding tissue was free of infection for 3 months after surgery (data not shown). These observations indicated that this novel mouse model is reproducible and suitable for evaluating the pathophysiology of both acute and chronic osteomyelitis.

Serological evaluation. During the early phase of infection, the mean serum IL-6 and IL-1β levels in the infected group were elevated. The serum IL-6 level was significantly higher in the infected group than in the control group on day 7 ($P < 0.05$) (Fig. 4A). The mean serum level of IL-1β in the infected group was significantly higher on days 7 and 14 ($P < 0.05$) (Fig. 4B). On day 0.5 (12 h), the mean level of MCP-1 was significantly higher in the infected group than in the control group ($P < 0.001$) (Fig. 4C). The mean serum CRP level increased quickly in both groups and remained at 20 ng/ml for 3 days, after which the level remained significantly higher in the infected group on days 7, 14, and 21 ($P < 0.001$) (Fig. 5A). There appeared to be a direct correlation between the bacterial PI and the serum CRP level in the samples obtained on days 14 and 21 ($n = 3$ each), the chronic phase of infection ($r = 0.85$; $P < 0.05$) (Fig. 5B).

Flow cytometry. Flow cytometric analyses using anti-CD11b and anti-Gr1 MAbs showed the presence of granulocytes in the peripheral blood in both groups (Fig. 6). The proportion of SSC^{high} $CD11b^+$ granulocytes in the peripheral blood was significantly higher in the infected group than in the control group on days 7, 14, and 21 ($n = 4$ each) (Fig. 6C).

Histological analysis. On day 21, the femur bone marrow from the sham-treated mice contained the normal cellular components of bone marrow: megakaryocytes, erythroid cells, and myeloid cells. In contrast, on day 3, bacterial colonies were detected in the medullary cavity of the infected mouse femur, along with a marked infiltration of neutrophils. The bacterial colonies were Gram positive. New bone formation started beneath the periosteum on day 7. By day 21, new bone formation and trabecular bone resorption by osteoclasts were present. Manifestations of chronic osteomyelitis, such as sequestrum, new bone formation, and fibrosis, were prominent on day 28 (Fig. 7).

DISCUSSION

Osteomyelitis is a serious infectious disease characterized by progressive bone destruction and formation (1, 19). In most cases, chronic osteomyelitis requires the administration of antibiotic drugs for prolonged periods and sometimes surgical procedures. Recently, the incidence of serious nosocomial infection due to

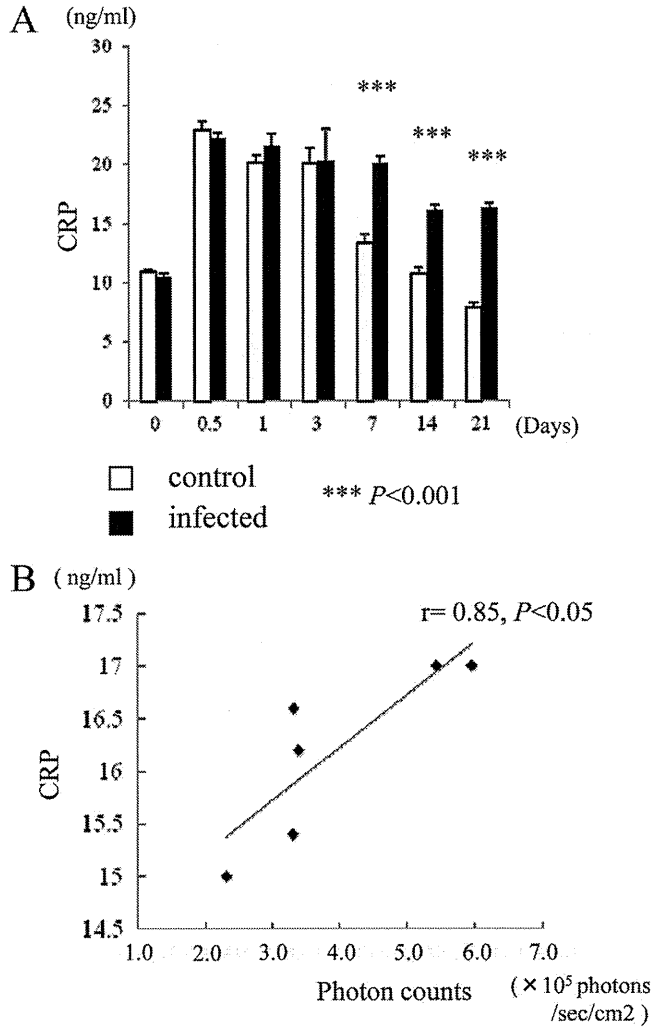

FIG 5 Serum CRP levels. (A) Correlations of bacterial photon intensity and the serum CRP level. The serum CRP levels in the infected and control groups were also measured with ELISA kits (n = 3 each). Shown are means ± SEM. (B) The bacterial CFU and bacterial PI are correlated. The serum CRP concentration was examined in the same samples from mice on days 14 (n = 3) and 21 (n = 3). A direct correlation between the bacterial PI and the serum CRP concentration was observed on both days (r = 0.85; $P < 0.05$).

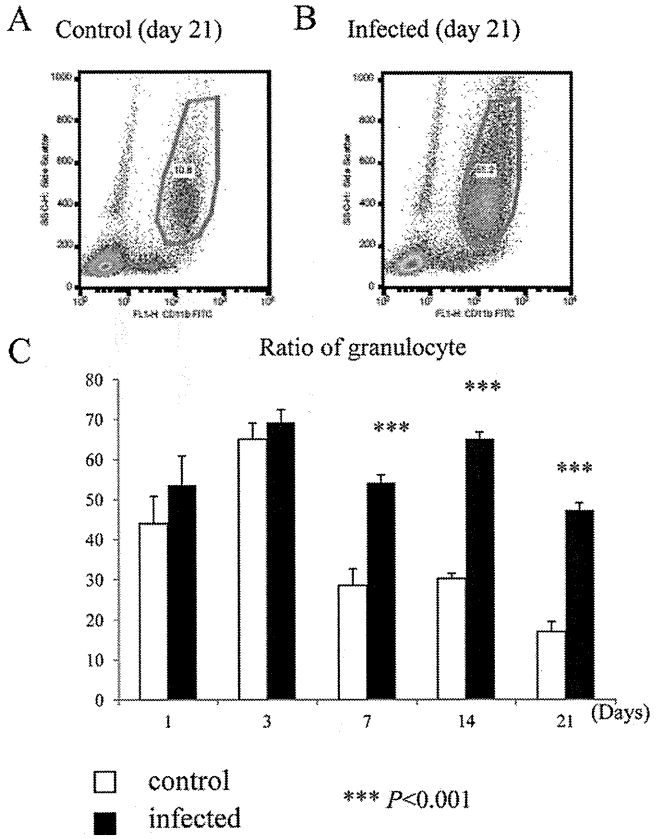

FIG 6 Proportion of granulocytes in the peripheral blood. (A and B) Peripheral blood samples were analyzed by flow cytometry on days 0.5 (12 h), 1, 3, 7, 14, and 21 after the operation in the infected and the control groups. Flow cytometric analyses of SSC^{high} $CD11b^{+}$ granulocytes in the peripheral blood of the control (A) and infected (B) mice on day 21 are shown. (C) The proportions of SSC^{high} $CD11b^{+}$ granulocytes in the peripheral blood on days 7, 14, and 21 were significantly higher in the infected group than in the control group (n = 4 each). Shown are means and SEM.

multiple-drug-resistant strains of bacteria has risen. Thus, the treatment of osteomyelitis has become more difficult (32, 44). Additional sources of rapidly spreading infections include orthopedic implants, such as those used in fracture fixations, arthroplasty, and spinal surgery (8, 39). A number of infection models have been created to study the diagnosis and treatment of osteomyelitis. For example, some investigators have attempted to implant staphylococci intravenously or directly into the bone. Although they successfully produced bone infections, these lesions were not progressive enough to simulate human osteomyelitis (31). Scheman et al. (35) established a reproducible model of chronic osteomyelitis in rabbits by injecting sodium morrhuate and *S. aureus* directly into the tibial metaphysis. Experimental models using small animals, such as rats and mice, allow easy handling and are cost-effective; in particular, mice are especially useful for understanding the pathophysiology of osteomyelitis because various genetically modified mice are commercially available. In recent papers, tibia infection mouse models have been used to evaluate implant-associated osteomyelitis (20, 36). However, because the mouse has tibial curvature with a short medullary cavity and scant surrounding soft tissue, the preparation of this model is technically difficult and often associated with incidental tibial fractures or leakage of the inoculated bacteria. In comparison, our novel osteomyelitis model using the mouse femur is easy and reproducible, because the medullary cavity is straight, with a long, thick cortex and adequate soft tissues surrounding the bone.

In previous animal models of osteomyelitis, the animals had to be sacrificed to quantify the bacterial burden and to assess the extent of infection and inflammation (7). Experiments using such models are very time-consuming, and there is an increased possibility of technical errors during sampling. Furthermore, since the animals have to be sacrificed at certain time points, it is impossible to monitor the same animal throughout the course of the infection. In contrast, recently developed BLI techniques enable us to monitor sequential gene expression patterns and the viabilities of the implanted cells or inoculated bacteria throughout the course of diseases without sacrificing the animal. Moreover, appropriately prepared animals can be selected at the outset of the experi-

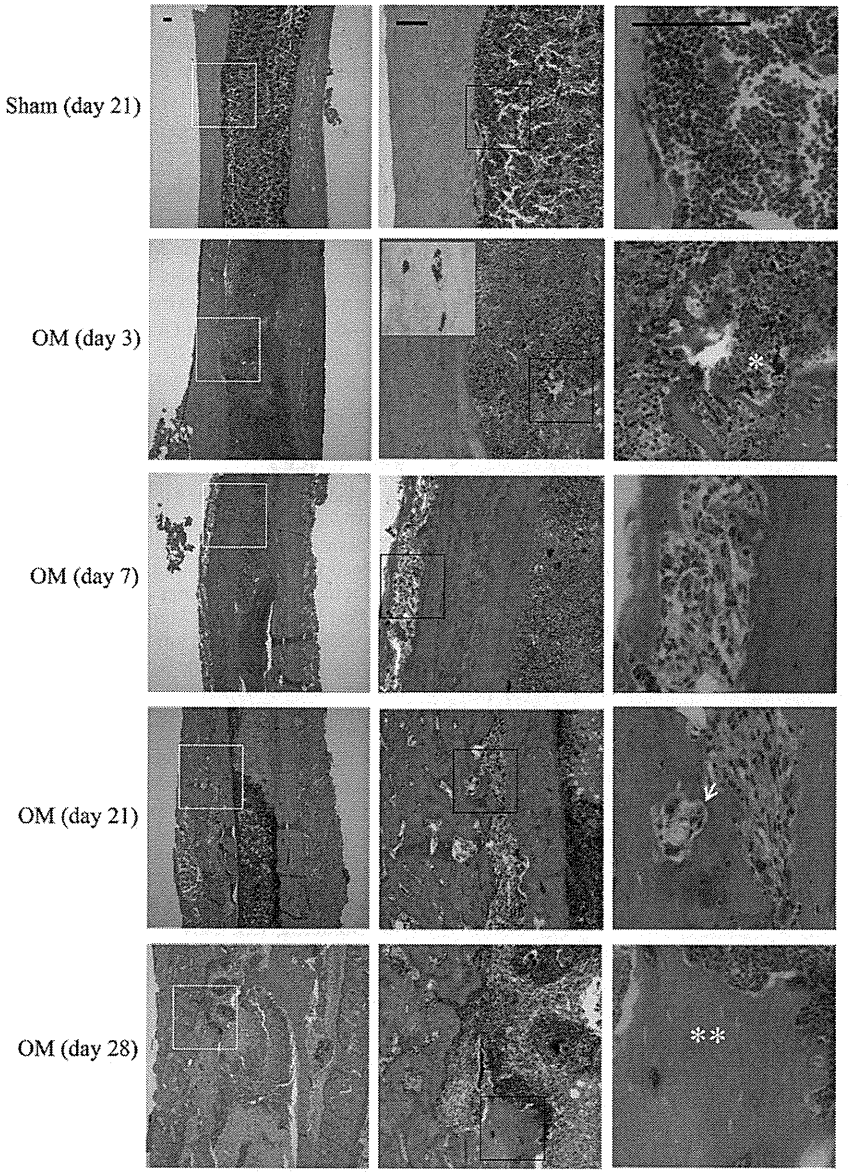

FIG 7 Changes over time in the histology of femurs from infected and control mice. Shown are hematoxylin and eosin staining of longitudinal sections of the uninfected and infected femurs on days 3, 7, 21, and 28 after bacterial inoculation. The middle and right images show higher-power views of the white-boxed areas of the left images and black-boxed areas of the middle images, respectively. The inset of the infected femur (day 3) indicates Gram-stain-positive bacteria. *, necrotic area with bacterial colonies; arrows, osteoclasts; **, sequestrum. Both acute and chronic manifestations of osteomyelitis were observed in this model. Bars = 100 μm.

ment, because the bacterial bioluminescence is visible and can be quantified immediately, thus enabling the accurate evaluation of a treatment and avoiding unnecessary follow-ups. Several studies have shown the advantages of *in vivo* BLI for the real-time monitoring of bacterial infections and their treatment (2, 5, 11, 14, 20, 24, 34, 42). In our mouse osteomyelitis model, sequential analysis of the bacterial luminescence revealed that the bacterial signal peaked on day 3 after the inoculation and then plateaued until day 7 and could be visualized for over 3 months. This time course is similar to that in the previous osteomyelitis models (2, 20), in which the innate immune system contributes to inhibiting the growth of the bacteria at the early phase (20). Recently, Bernthal et al. (2) established a mouse model of implant-associated infection as a preclinical screening tool. However, a limitation of their model is the use of the SH1000 *S. aureus* bioluminescent strain, in which the *lux* genes are contained in a plasmid. The plasmid is stable for only the first 3 days of broth culture, so it is difficult to estimate bacterial numbers by the bioluminescent signals of the strain after 3 days. Thus, their model represents only acute, not chronic, infection. In our model, the *lux* genes were inserted into the *S. aureus* chromosome and the bioluminescent signals were maintained for a longer period. In addition, leakage of the inoculated bacteria to surrounding tissues is often observed in implant-associated osteomyelitis and joint infection models and can be a major cause of skin ulcers. Such models are poorly reproducible, with short, unstable emission of the bacterial luminescence. In

contrast, the pinhole created in the femur for bacterial inoculation in our model closed spontaneously and rapidly enough to keep the bacterial infection contained inside the medullary cavity of the femur. In fact, a strong bacterial bioluminescent signal was detected for over 3 months after inoculation in our model.

In the present study, the mean serum IL-6 and IL-1β concentrations in the infected group were significantly higher than those in the control group. Marriott et al. (22) demonstrated that osteoblasts express IL-6 during bacterial bone infection in a mouse model and in human bone tissues. IL-6 (12, 17) and IL-1β (4, 25), which are produced by stimulated monocytes/macrophages, stimulate osteoclasts and lead to bone resorption. Yoshii et al. reported that the local levels of IL-6 and IL-1β in the infected bone were elevated in the early postinfection period in a staphylococcal osteomyelitis model. They suggested that the elevated IL-6 and IL-1β levels induced by infection may be related to bone damage mainly in the early phase of infection (43). Our results also demonstrated that the mean serum IL-6 and IL-1β concentrations in the infected group were significantly higher at the time pathological changes, such as new bone formation beneath the periosteum, appeared (approximately on day 7). The serum CRP levels in both groups were elevated during the first 3 days (days 0.5, 1, and 3), after which the high level of CRP in the infected group was prolonged through day 7. The elevated CRP level in the early phase might have been caused by the surgical invasion. However, the elevated level was sustained in the infected group for a longer period. The CRP level is one of the most valuable markers for evaluating infectious processes in the clinical field (10, 15, 40). In this study, there was a high correlation between the CRP level and bacterial PI *in vivo* during the chronic phase, suggesting that our model is useful for real-time, noninvasive monitoring of the chronic inflammatory processes in osteomyelitis. In contrast, the mean serum level of MCP-1 was significantly higher in the infected group on day 0.5 (12 h). Cultured osteoblasts produce high MCP-1 levels in response to *S. aureus*, leading to a proposal that MCP-1 causes the inflammation that results in progressive bone destruction (3, 9). Marriott et al. (23) reported that increased MCP-1 is the pivotal inflammatory chemokine during *S. aureus*-associated osteomyelitis *in vivo*. We also demonstrated here that the proportion of granulocytes in the peripheral blood was significantly higher in the infected group than in the control group after day 7, suggesting that granulocytes are induced by chemokine activities during the early phase and that systemic infection due to osteomyelitis was maintained during the chronic phase. Thus, the present osteomyelitis model mimics the infectious processes in humans well.

Additionally, the histological study also demonstrated the reproducibility of the present model. The histological analysis showed new bone formation beneath the periosteum at the early phase and trabecular bone resorption by osteoclasts and fibroblast proliferation during the chronic phase, demonstrating the pathological features of chronic osteomyelitis.

In conclusion, we have successfully visualized and quantified bacterial growth in a mouse osteomyelitis model using *in vivo* BLI. We were able to monitor the infectious processes throughout the course of the disease in both the acute and chronic phases without sacrificing the animals. To our knowledge, this is the first report describing a real-time, quantitative, and reproducible model for both acute and chronic osteomyelitis of the mouse femur with kinetics of immune cells and serum cytokine/chemokine levels. This novel, quantitative, and reproducible model can be used to clarify the pathology and kinetics of osteomyelitis and to evaluate novel *in vivo* therapeutic strategies, including the development of new antibiotics and bacterium-resistant implants, before performing studies in larger animals and human subjects.

ACKNOWLEDGMENTS

We thank Y. Baba for technical assistance with the serological analyses.

This work was supported by a grant from the Japan Orthopaedics and Traumatology Foundation, Inc. (no.192); Keio Gijuku Academic Development Funds; and the General Insurance Association of Japan, Health Labor Sciences Research Grant and Research for Promoting Technological Seeds.

S.K. is a consultant for Medical and Biological Laboratories Co., Ltd. We have no other financial conflicts of interest.

REFERENCES

1. **Aliabadi P, Nikpoor N.** 1994. Imaging osteomyelitis. Arthritis Rheum. 37:617–622.
2. **Bernthal NM, et al.** 2010. A mouse model of post-arthroplasty Staphylococcus aureus joint infection to evaluate in vivo the efficacy of antimicrobial implant coatings. PLoS One 5:e12580.
3. **Bost KL, et al.** 2001. Monocyte chemoattractant protein-1 expression by osteoblasts following infection with Staphylococcus aureus or Salmonella. J. Interferon Cytokine Res. 21:297–304.
4. **Boyce BF, Aufdemorte TB, Garrett IR, Yates AJP, Mundy GR.** 1989. Effects of interleukin-1 on bone turnover in normal mice. Endocrinology 125:1142–1150.
5. **Contag CH, et al.** 1995. Photonic detection of bacterial pathogens in living hosts. Mol. Microbiol. 18:593–603.
6. **Costa GL, et al.** 2001. Adoptive immunotherapy of experimental autoimmune encephalomyelitis via T cell delivery of the IL-12 p40 subunit. J. Immunol. 167:2379–2387.
7. **Cremieux AC, Carbon C.** 1997. Experimental models of bone and prosthetic joint infections. Clin. Infect. Dis. 25:1295–1302.
8. **Darouiche RO.** 2004. Treatment of infections associated with surgical implants. N. Engl. J. Med. 350:1422–1429.
9. **Dean RA, et al.** 2008. Macrophage-specific metalloelastase (MMP-12) truncates and inactivates ELR+ CXC chemokines and generates CCL2, -7, -8, and -13 antagonists: potential role of the macrophage in terminating polymorphonuclear leukocyte influx. Blood 112:3455–3464.
10. **Du Clos TW.** 2000. Function of C-reactive protein. Ann. Med. 32:274–278.
11. **Francis KP, et al.** 2000. Monitoring bioluminescent *Staphylococcus aureus* infections in live mice using a novel *luxABCDE* construct. Infect. Immun. 68:3594–3600.
12. **Ishimi Y, et al.** 1990. IL-6 is produced by osteoblasts and induces bone resorption. J. Immunol. 145:3297–3303.
13. **Johansson A, Svensson O, Blomgren G, Eliasson G, Nord CE.** 1991. Anaerobic osteomyelitis. A new experimental rabbit model. Clin. Orthop. 265:297–301.
14. **Kadurugamuwa JL, et al.** 2003. Rapid direct method for monitoring antibiotics in a mouse model of bacterial biofilm infection. Antimicrob. Agents Chemother. 47:3130–3137.
15. **Khan MH, Smith PN, Rao N, Donaldson WF.** 2006. Serum C-reactive protein levels correlate with clinical response in patients treated with antibiotics for wound infections after spinal surgery. Spine J. 6:311–315.
16. **Kim DE, Schellingerhout D, Ishii K, Shah K, Weissleder R.** 2004. Imaging of stem cell recruitment to ischemic infarcts in a murine model. Stroke 35:952–957.
17. **Kurihara N, Bertolini D, Suda T, Akiyama Y, Roodman GD.** 1990. IL-6 stimulates osteoclast-like multinucleated cell formation in long term human marrow cultures by inducing IL-1 release. J. Immunol. 144:4226–4230.
18. **Kurtz SM, et al.** 2007. Future clinical and economic impact of revision total hip and knee arthroplasty. J. Bone Joint Surg. Am. 89:144–151.
19. **Lew DP, Waldvogel FA.** 2004. Osteomyelitis. Lancet 364:369–379.
20. **Li D, et al.** 2008. Quantitative mouse model of implant-associated osteomyelitis and the kinetics of microbial growth, osteolysis, and humoral immunity. J. Orthop. Res. 26:96–105.

21. **Mandl S, Schimmelpfennig C, Edinger M, Negrin RS, Contag CH.** 2002. Understanding immune cell trafficking patterns via in vivo bioluminescence imaging. J. Cell Biochem. Suppl. **39**:239–248.
22. **Marriott I, et al.** 2004. Osteoblasts express the inflammatory cytokine interleukin-6 in a murine model of *Staphylococcus aureus* osteomyelitis and infected human bone tissue. Am. J. Pathol. **164**:1399–1406.
23. **Marriott I, et al.** 2005. Osteoblasts produce monocyte chemoattractant protein-1 in a murine model of Staphylococcus aureus osteomyelitis and infected human bone tissue. Bone **37**:504–512.
24. **Mortin LI, et al.** 2007. Rapid bactericidal activity of daptomycin against methicillin-resistant and methicillin-susceptible *Staphylococcus aureus* peritonitis in mice as measured with bioluminescent bacteria. Antimicrob. Agents Chemother. **51**:1787–1794.
25. **Nishihara T, Ishihara Y, Noguchi T, Koga T.** 1989. Membrane IL-1 induces bone resorption in organ culture. J. Immunol. **143**:1881–1886.
26. **Norden CW.** 1970. Experimental osteomyelitis. I. A description of the model. J. Infect. Dis. **122**:410–418.
27. **Okada S, et al.** 2005. In vivo imaging of engrafted neural stem cells: its application in evaluating the optimal timing of transplantation for spinal cord injury. FASEB J. **19**:1839–1841.
28. **Pillon A, Servant N, Vignon F, Balaguer P, Nicolas JC.** 2005. In vivo bioluminescence imaging to evaluate estrogenic activities of endocrine disrupters. Anal. Biochem. **340**:295–302.
29. **Pucci F, et al.** 2009. A distinguishing gene signature shared by tumor-infiltrating Tie2-expressing monocytes, blood "resident" monocytes, and embryonic macrophages suggests common functions and developmental relationships. Blood **114**:901–914.
30. **Rice BW, Cable MD, Nelson MB.** 2001. In vivo imaging of light-emitting probes. J. Biomed. Opt. **6**:432–440.
31. **Rissing JP.** 1990. Animal models of osteomyelitis. Knowledge, hypothesis, and speculation. Infect. Dis. Clin. North Am. **4**:377–390.
32. **Rissing JP.** 1997. Antimicrobial therapy for chronic osteomyelitis in adults: role of the quinolones. Clin. Infect. Dis. **25**:1327–1333.
33. **Rissing JP, Buxton TB, Weinstein RS, Shockley RK.** 1985. Model of experimental chronic osteomyelitis in rats. Infect. Immun. **47**:581–586.
34. **Sadikot RT, et al.** 2001. High-dose dexamethasone accentuates nuclear factor-kappa b activation in endotoxin-treated mice. Am. J. Respir. Crit. Care Med. **164**:873–878.
35. **Scheman L, Janota M, Lewin P.** 1941. The production of experimental osteomyelitis: preliminary report. JAMA **177**:1525–1529.
36. **Schmidmaier G, Lucke M, Wildemann B, Haas NP, Raschke M.** 2006. Prophylaxis and treatment of implant-related infections by antibiotic-coated implants: a review. Injury **37**:S105–S112.
37. **Sever D, et al.** 2011. Evaluation of impaired beta-cell function in nonobese-diabetic (NOD) mouse model using bioluminescence imaging. FASEB J. **25**:676–684.
38. **Sweeney TJ, et al.** 1999. Visualizing the kinetics of tumor-cell clearance in living animals. Proc. Natl. Acad. Sci. U. S. A. **96**:12044–12049.
39. **Toms AD, Davidson D, Masri BA, Duncan CP.** 2006. The management of peri-prosthetic infection in total joint arthroplasty. J. Bone Joint Surg. Br. **88**:149–155.
40. **Volanakis JE.** 2001. Human C-reactive protein: expression, structure, and function. Mol. Immunol. **38**:189–197.
41. **Wang X, et al.** 2003. Dynamic tracking of human hematopoietic stem cell engraftment using in vivo bioluminescence imaging. Blood **102**:3478–3482.
42. **Wiles S, Pickard KM, Peng K, MacDonald TT, Frankel G.** 2006. In vivo bioluminescence imaging of the murine pathogen *Citrobacter rodentium.* Infect. Immun. **74**:5391–5396.
43. **Yoshii T, et al.** 2002. Local levels of interleukin-1β, -4, -6, and tumor necrosis factor in an experimental model of murine osteomyelitis due to *Staphylococcus aureus.* Cytokine **19**:59–65.
44. **Zinner SH.** 1999. Changing epidemiology of infections in patients with neutropenia and cancer: emphasis on gram-positive and resistant bacteria. Clin. Infect. Dis. **29**:490–494.

特集1

脊髄損傷治療の現状とこれから

人工多能性幹（iPS）細胞を用いた脊髄損傷治療

安田明正[1,2]，辻　収彦[1]，藤吉兼浩[1,3]，戸山芳昭[1]，岡野栄之[2]，中村雅也[1]

1) 慶應義塾大学医学部整形外科学教室（〒160-8582 東京都新宿区信濃町35）E-mail：yasuda@z7.keio.jp
2) 慶應義塾大学医学部生理学教室
3) 独立行政法人国立病院機構村山医療センター整形外科

SUMMARY

損傷脊髄の再生は困難であると考えられてきたが，幹細胞研究の急速な進歩により，細胞移植治療が脚光を浴びるようになってきた．胎児（胎仔）やES細胞由来神経幹/前駆細胞が脊髄損傷に対する移植細胞として期待されていたが，倫理的・免疫学的問題から臨床応用へ踏み切るのは難しい状態である．成体組織から採取した線維芽細胞で樹立しうるiPS細胞が2006年に報告され，以降，当研究室ではiPS細胞を用いた脊髄損傷治療の検討を行ってきた．我々は，免疫不全マウスへの移植実験で腫瘍化のリスクが低いことが確認できたマウスiPS細胞由来の神経幹/前駆細胞をマウス脊髄損傷モデルへ移植し，その有効性を確認することができた．しかし，腫瘍化能の高いiPS細胞クローン由来の神経幹/前駆細胞は移植後に損傷脊髄内で奇形腫を形成した．iPS細胞関連の研究は著しく進歩しているが，安全性を評価しつつ有効性を検討することが肝要である．

KEY WORDS

脊髄損傷
人工多能性幹（iPS）細胞
神経幹/前駆細胞
胚性幹（ES）細胞
腫瘍化

本項では，これまで行われてきた脊髄損傷に対する細胞移植研究，さらには我々が行ってきたiPS(induced pluripotent stem: iPS) 細胞を用いた研究について概説し，最後にiPS細胞関連の研究における問題点と今後の展望に関しても言及したい．

I. 胎児（胎仔）および胚性幹（embryonic stem: 以下ES）細胞由来神経幹/前駆細胞を用いた脊髄損傷治療の検討

中枢神経である脊髄は，再生能力が非常に低く，一度損傷を受けると再生は困難であると考えられてきた．近年，幹細胞研究の急速な進歩により，動物実験レベルでは，細胞移植をはじめ，損傷脊髄の修復が得られる治療法が多数報告されるようになった．基礎研究で得られた結果を臨床の現場で応用できれば，脊髄損傷に対して新たな治療法を確立することも夢ではないと考えられる．

細胞移植は古くから注目を集めており，1980年代にスウェーデンLund大学のLindvallのグループが，パーキンソン病患者の脳へ胎児中脳を移植し，機能の回復が得られることを報告した[1]．その後，脊髄損傷に対しても，胎児脊髄移植の有効性が示された[2,3]．しかし，胎児組織の移植には多くを一度に得られない量的制約などが問題となり，神経幹細胞が脚光を浴びるようになった．

1344-0128/11/ ¥100/JCOPY

a) 神経幹/前駆細胞

神経幹/前駆細胞（NS/PC）とは，中枢神経系を構成するニューロンやグリア細胞へ分化する多分化能を有し，自己複製能も持つ未分化な細胞である．1992年にReynoldsとWeissにより，NS/PCを効率よく増殖できるneurosphere法が報告され[4]，必要十分量の細胞数を*in vitro*で増殖させることが可能となり，細胞移植材料として期待されるようになった．

当研究室でも脊髄損傷治療の研究において，ラット胎仔脊髄由来NS/PC移植のラット脊髄損傷への有効性[5]，さらにはヒト胎児前脳由来NS/PC移植の霊長類コモンマーモセット脊髄損傷モデルへの有効性[6,7]を報告してきた．いずれも，運動機能の回復および組織学的評価において良好な結果が得られたことから，胎仔/胎児由来NS/PCは脊髄損傷治療に非常に有用な移植細胞と考えてきた．しかし，脊髄損傷患者への臨床応用を考慮すると，中絶胎児からの細胞採取が必要となるため，倫理的観点から現時点ではわが国において臨床応用の実現は不可能といわざるを得ない．

b) ES細胞

胚性幹（embryonic stem: 以下ES）細胞は，受精卵の胚盤胞期の胚の一部である内細胞塊から作製される細胞で，理論上すべての細胞になる能力を有することから“万能細胞”ともいわれる．神経組織も含む胎児の全細胞は内細胞塊に由来しており，脊髄損傷治療の研究においても注目されてきた．1999年にはMcDonaldらがES細胞から形成したNS/PCをラット損傷脊髄へ移植し，良好な機能回復を報告し[8]，2005年にはKeirsteadらがヒトES細胞から高純度へ誘導したオリゴデンドロサイト前駆細胞のラット脊髄損傷モデルへの移植で，損傷脊髄内で脱髄した軸索の再髄鞘化と後肢の機能回復を報告している[9]．当研究室においてもマウスES細胞由来NS/PCを用いたマウス脊髄損傷治療の検討を行い，その有効性を確認した[10]．しかし，ES細胞の作製には精子と卵子が結合した後の受精卵が必要となり，不妊治療で生じた余剰胚を用いるとはいえ，臨床応用を考えると倫理的な問題が避けられない．（ES細胞由来のオリゴデンドロサイト前駆細胞移植については，2010年10月に米国Geron社が実際に脊髄損傷患者への臨床試験を行ったと発表しており，世界的な注目を集めている[11]．）

c) 免疫拒絶反応

胎児およびES細胞由来NS/PCを移植治療に用いる際，通常では他人の細胞を移植するallograftとなるため，免疫拒絶反応が起こる可能性がある．拒絶反応には臓器障害を含む患者の全身反応も含まれるが，中枢神経においても他の臓器と同様に，MHC（主要組織適合遺伝子複合体）の違いによる免疫拒絶により組織の生着を妨げる[12,13]．脊髄損傷に対する細胞移植後の機能回復には，移植細胞からの液性因子のみならず，生着し分化した細胞が関与しているという報告が近年散見されており[14]，細胞移植治療における免疫拒絶の問題は臨床応用を阻む大きな要因となっている．

II. iPS細胞を用いた脊髄損傷治療

これまで述べたような諸問題に解決の糸口を与えたのが，2006年，2007年に京都大学山中伸弥教授らにより，それぞれマウス，ヒトの線維芽細胞より樹立された人工多能性幹細胞（induced pluripotent stem cell: 以下iPS細胞）である[15,16]．iPS細胞は，マウス/ヒト線維芽細胞に*Oct3/4*，*Sox2*，*Klf4*，（*c-Myc*）などの初期化遺伝子を導入しリプログラミングすることで，ES細胞と同等の増殖能・分化能を持った多能性幹細胞である．iPS細胞は患者自身の体細胞から樹立することが可能であるため，先に述べた倫理的問題・免疫拒絶反応などの問題を解決する技術として期待されている．当研究室では，マウスES細胞のNS/PCへの誘導培養法[17]をマウスiPS細胞[18]に応用し，ニューロン，アストロサイト，オリゴデンドロサイトへの分化を確認した．脊髄損傷に対するマウスES細胞由来NS/PCの治療効果をすでに確認していたことから，iPS細胞でも同様の効果が期待できる．しかし，iPS細胞における最も大きな問題である移植細胞による腫瘍化の検討が重要と考え，以下の研究を行った．

a) iPS細胞由来の神経幹/前駆細胞の安全性

これまで脊髄損傷モデルへの移植検討を行ってきたiPS細胞では，ウイルス等による染色体への外来遺伝子挿入による遺伝子変異からES細胞にも増して腫

癌化の危険性が危惧される．そこで三浦らは，36種類の個別に独立したマウスiPS細胞株よりNS/PCを分化誘導し，その安全性の検討を行った[19]．腫瘍形成能と樹立時の*c-Myc*遺伝子の有無や薬剤選択の有無との相関についての解析では，予想と反して前癌遺伝子である*c-Myc*の有無とは腫瘍形成能との相関は無く，統計学的有意差があったのはiPS細胞樹立時の起源細胞（origin）のみであった．つまり，腫瘍形成能はiPS細胞が胎児由来（例，mouse embryonic fibroblast: MEF由来）か成体由来であるか（例，tail tip fibroblast: TTF由来）によって最も強く規定されていた[19]．臨床応用に向けては，成体由来細胞を用いてiPS細胞を樹立して移植療法を目指すのが理想的ではあるが，成体由来iPS細胞はより腫瘍形成をしやすいという結果となった．また，成体由来iPS細胞より低いとはいえ，胎児由来iPS細胞にも腫瘍形成を示すものが存在し，ニューロスフェアまで分化誘導した際に残存する分化抵抗性の未分化細胞の比率が腫瘍形成と関連していた．iPS細胞由来NS/PCによる移植治療に向けては，未分化細胞がほとんど含まれておらず，且つ免疫不全マウス大脳への移植実験を経て24週間にわたって腫瘍を全く形成しなかった，“安全な”クローンを選ぶことが重要である．

b) iPS細胞由来NS/PCの脊髄損傷モデルへの有効性

前述の24週間にわたり腫瘍を全く形成しなかった“安全な”クローンのうち，まずマウス胎仔由来線維芽細胞MEF由来のクローンから作製されたニューロスフェアを用いて，当研究室では脊髄損傷モデルマウスへの移植実験を行った[20]．雌の8週齢C57Bl6/Jマウスを用いて，損傷は第10胸椎高位にI-H impactorを用いてコンピュータ制御下に圧挫損傷を作製し，損傷後亜急性期となる9日目に5×10^5個を損傷中心部へと移植した．移植細胞にはレンチウイルスを用いて，移植前にホタル発光酵素ルシフェラーゼの一種であるCBRluc遺伝子と，赤色蛍光タンパク質遺伝子mRFPを導入することで，移植細胞の生存をルシフェラーゼ発光によるバイオイメージングを用いて動物生存下に経時的モニタリングを行い，損傷後6週間の観察ののち組織学的検討を行った．その結果，移植細胞はバイオイメージングを用いた定量的評価により，移植後5週の時点で約20%が生着しており，明らかな発光量の増大は認めず，組織学的検討においても腫瘍形成を認めなかった．移植細胞はHu陽性のニューロン，GFAP陽性のアストロサイト，GST-π陽性のオリゴデンドロサイトへと分化しており，分化効率はそれぞれニューロンが約30%，アストロサイトが約50%，オリゴデンドロサイトが約15%であった．マウスの後肢運動機能をBasso Mouse Scale（以下BMS）を用いた運動機能評価では，iPS細胞由来NS/PC移植群はマウスES細胞由来NS/PC移植群とほぼ同等の回復を示し，後肢で体幹を支持しながら歩行できるまでに改善していた．一方，培養液のみを注入したvehicle control群では後肢で体幹を支持できなかった．以上より，iPS細胞由来NS/PC移植により有意な下肢運動機能回復が得られることが明らかとなった．移植されたiPS細胞由来NS/PCがMBP陽性の成熟オリゴデンドロサイトへと分化し，損傷により脱髄した神経線維を再髄鞘化していた（**図1**）．LFB染色でも損傷部髄鞘面積がvehicle control群と比較して，iPS細胞由来NS/PC移植群で有意に増加していた．また，移植細胞が双極性の突起を持つ幼若アストロサイトへと損傷脊髄内で分化し，軸索再生のガイダンスとして働いた可能性が考えられた．事実，この幼若アストロサイトの近傍に運動機能に大きな役割を持つとされる5-HT陽性の縫線核脊髄路神経線維が多数存在しており，損傷部から4 mm遠位部での定量で5-HT陽性線維は，移植群において有意に増加していた[20]．以上の結果より，移植細胞による再髄鞘化と縫線核脊髄路線維へのglial supportが，iPS由来NS/PC移植による後肢機能回復の主なメカニズムであることが示唆された．

c) 成体組織由来の“安全な”iPS細胞クローンと“危険な”iPS細胞クローンの比較

自家組織からの移植が可能となれば，iPS細胞を用いた脊髄損傷治療の実現に向けた大きな一歩となる．そのためより現実的なモデルである成体組織（TTF）由来のiPS細胞を用いて同様の移植実験を行った．三浦らが行った安全性の検討において使用したマウスiPS細胞36クローンのうち，TTF由来のクローンは6クローンあったが，そのうち安全性が確認でき